Geophysical Research Letters

Key Points:

- Surface-towed marine-controlled source electromagnetic technique is capable of imaging freshwater plumes in high-resolution
- Multiple large-scale freshwater plumes and surface freshwater bodies were detected offshore the island of Hawai'i
- Substantial volumes of freshwater occupy seafloor to ocean surface plumes in west Hawai'i

Supporting Information:

- Supporting Information S1

Correspondence to:

E. Attias,
attias@hawaii.edu

Marine Electromagnetic Imaging and Volumetric Estimation of Freshwater Plumes Offshore Hawai'i

Eric Attias[1] , Steven Constable[2] , Dallas Sherman[3], Khaira Ismail[4] , Christopher Shuler[5] , and Henrietta Dulai[6]

[1]Hawai'i Institute of Geophysics and Planetology, School of Ocean and Earth Science and Technology, University of Hawai'i at Mānoa, Honolulu, HI, USA, [2]Scripps Institution of Oceanography, University of California San Diego, San Diego, CA, USA, [3]Frontier Geosciences, Vancouver, BC, Canada, [4]Universiti Malaysia Terengganu, Kuala Nerus, Malaysia, [5]Water Resources Research Center, University of Hawai'i at Mānoa, Honolulu, HI, USA, [6]Department of Earth Sciences, School of Ocean and Earth Science and Technology, University of Hawai'i at Mānoa, Honolulu, HI, USA

Abstract Submarine groundwater discharge (SGD) is an important phenomenon that governs hydrological cycles at the land-to-ocean transition zone. SGD manifests as cold and buoyant freshwaters influx from the seafloor to the water column that contains carbon, nutrients, metals, and greenhouse gases, altering coastal areas' oceanographical and biochemical properties. Here, we present electromagnetic imaging of large-scale freshwater plumes in high-resolution, offshore west Hawai'i. Electrical resistivity models detect multiple vertical freshwater plumes extending from the seafloor to the ocean surface. Additionally, our models image extensive spatially distributed surface freshwater. The resistivity of these plumes and surface freshwater ranges from ∼1 to 30 Ωm. Resistivity-to-salinity calculation indicates a plume-scale salinity range of ∼0.3–9.9, containing up to 87% of freshwater. Our results imply that substantial volumes of freshwater occupy water column plumes in Hawai'i. This study offers a new and effective method to elucidate hydrogeologic and ocean processes affecting biogeochemical cycles in coastal waters worldwide.

Plain Language Summary Submarine groundwater discharge (SGD) is a flow of cold and buoyant freshwater from the seafloor to the ocean surface. Because SGD contains carbon, nutrients, metals, and greenhouse gases, it changes coastal waters' oceanographical and biochemical properties. Therefore, SGD is an important phenomenon that governs hydrological cycles at the land-to-ocean transition zone. Due to the high spatial distribution and variability of SGD at the ocean surface, it is nontrivial to map SGD seep location and fluxes using traditional oceanographic methods. Here, we present electromagnetic imaging of large-scale freshwater plumes in high-resolution, offshore west Hawai'i. Our electrical resistivity models detect multiple vertical freshwater plumes (SGD point-sources) as well as spatially distributed surface freshwater, extending to a distance of ∼3 km offshore Hawai'i. Plume-scale salinity distribution indicates that these plumes contain up to 87% of freshwater. Thus, a substantial volume of freshwater occupies Hawaiian water column plumes. This is the first study to demonstrate the marine electromagnetic method's capability to image and delineate freshwater plumes from the seafloor to the ocean surface. We offer a new and effective method to elucidate hydrogeologic and ocean processes that affect biogeochemical cycles in coastal waters worldwide.

1. Introduction

Freshwater resources are essential for preserving public health, agricultural yields, economic strategies, and ecosystem functions (Gleick & Palaniappan, 2010; Michael et al., 2017). As populations and economies grow, new constraints on water resources emerge that may limit global water availability (Gleick & Palaniappan, 2010). Optimized groundwater systems' characterization and seeking alternative freshwater resources are vital to address the increasing demand worldwide. Hence, such demand positions groundwater research at the center of broad interdisciplinary interest from industry, government, and academic organizations (e.g., Manzoor et al., 2020; Person et al., 2017). For the past decade, considerable evidence suggests that vast offshore groundwater reserves exist globally in submarine provinces extending far beyond their presumed coastal boundaries (Post et al., 2013; Micallef, Person, Berndt, et al., 2020). These offshore

groundwater reservoirs are more prevalent than initially thought, thus are being recognized as potential water resources for coastal communities (Bakken et al., 2012; Cohen et al., 2010; Jiao et al., 2015).

Actively recharged offshore submarine groundwater accumulations can sometimes manifest by a process known as submarine groundwater discharge (SGD), where fresh groundwater percolates upward from the sub-seafloor to the water column, altering ocean water salinity, temperature, and chemistry (e.g., Church, 1996; Kohout, 1966; Burnett et al., 2003; Moore, 2010). A recent estimate suggests that tropical coasts transport more than 56% of near-global fresh SGD (Zhou et al., 2019). The fresh portion of SGD is critical, as it potentially buffers ocean acidification with groundwater alkalinity (Cyronak et al., 2013; Slomp & Van Cappellen, 2004). While coastal SGD has been documented globally at various geological settings (Kim & Kim, 2011; Knee et al., 2016; Paldor et al., 2020; Prakash et al., 2018; Stieglitz, 2005), reports on deep offshore SGD sources (disconnected from coastal SGD, usually appear at water depths >50 m) are scarce but of potential importance. Fresh SGD is commonly associated with oceanographic, hydrogeological, and environmental processes that affect chemical weathering, ocean eutrophication, and climate change by emanating solutes and gases to the ocean (e.g., Moore, 2010; Kim & Kim, 2011; Taniguchi et al., 2019; Luijendijk et al., 2020). Hence, SGD has societal importance for coastal communities (Moosdorf & Oehler, 2017).

The locations and rates of nearshore/offshore SGD are essential to define boundary conditions in coastal aquifer models and quantify the nutrients and contaminants transported to the marine environment (e.g., W. S. Moore, 1996; Duarte et al., 2006). Fresh SGD in coastal waters affects stable isotope levels (Mayfield et al., 2021) and global carbon budgets (e.g., Maher et al., 2013). Ecosystems ranging from plankton to fish benefit from SGD, exhibiting enhanced productivity and fish abundance near groundwater springs due to favorable temperature, nutrient content, and oxygen levels of the discharged groundwater (e.g., Fujita et al., 2019; Slomp & Van Cappellen, 2004; Starke et al., 2020). Conversely, nutrient-rich SGD causes increased phytoplankton and macroalgae growth, reduction of seagrass beds and associated fauna (e.g., Paerl, 1997; Valiela et al., 1990), as well as Mercury contamination of fish habitats (Black et al., 2009). Thus, SGD alters species diversity and marine habitats' dynamics.

SGD is commonly studied using various geophysical, geochemical, bioecological, and numerical simulation methods, utilizing seepage meters and hydraulic gradient observations (e.g., Burnett et al., 2006; Moore, 2010; Taniguchi et al., 2019; Rosenberry et al., 2020). Nevertheless, it is nontrivial to produce regional SGD maps in high-resolution due to extensive spatiotemporal variability of fluxes, ranging from focused springs to broad seepage fields (e.g., Burnett et al., 2003; Burnett et al., 2006; Duarte et al., 2006; Luijendijk et al., 2020; Mayfield et al., 2021). Therefore, high-resolution field characterizations of SGD on regional scales are scarce. Thermal infrared imagery and geochemical tracer studies performed along the coast of west Hawai'i infer daily coastal groundwater discharge that varies between 1,100 and 13,700 m^3/d (Dulai et al., 2016; Johnson et al., 2008; Peterson et al., 2009). However, these studies only provide information about buoyant brackish/freshwater plumes discharging at the coastline, thus, neglecting offshore SGD. Therefore, offshore SGD locations, spatial plume distribution, and volumetric inventory from the seafloor to the ocean surface are poorly constrained offshore west Hawai'i as well as globally.

Freshwater is electrically resistive whereas seawater is conductive. Therefore, marine controlled-source electromagnetic (CSEM) methods have proven useful in imaging brackish/freshwater sub-seafloor accumulations at sedimentary regions (e.g., Evans & Key, 2016; Haroon et al., 2018; Gustafson et al., 2019; Micallef, Person, Haroon, et al., 2020), as they are sensitive to contrasts in bulk electrical resistivity resulting from alterations in pore water salinity (Edwards, 2005; S. Constable, 2010). However, CSEM data inversion has never been used to image freshwater plumes within the water column. Here, we employ a newly developed surface-towed CSEM system (Sherman et al., 2017) demonstrating for the first time the CSEM techniques' capability to image freshwater plumes in high-resolution on a local scale, as well as surface freshwater on a regional scale, offshore west of Hawai'i. Additionally, we present plume-scale salinity distribution and freshwater volumetric estimation.

1.1. Geologic and Oceanographic Setting

Extensive basaltic units in Hawai'i were formed consequently to volcanic eruptions during the initial building stage of each volcano (Gingerich & Oki, 2000). These volcanic eruptions are characterized by lava flows,
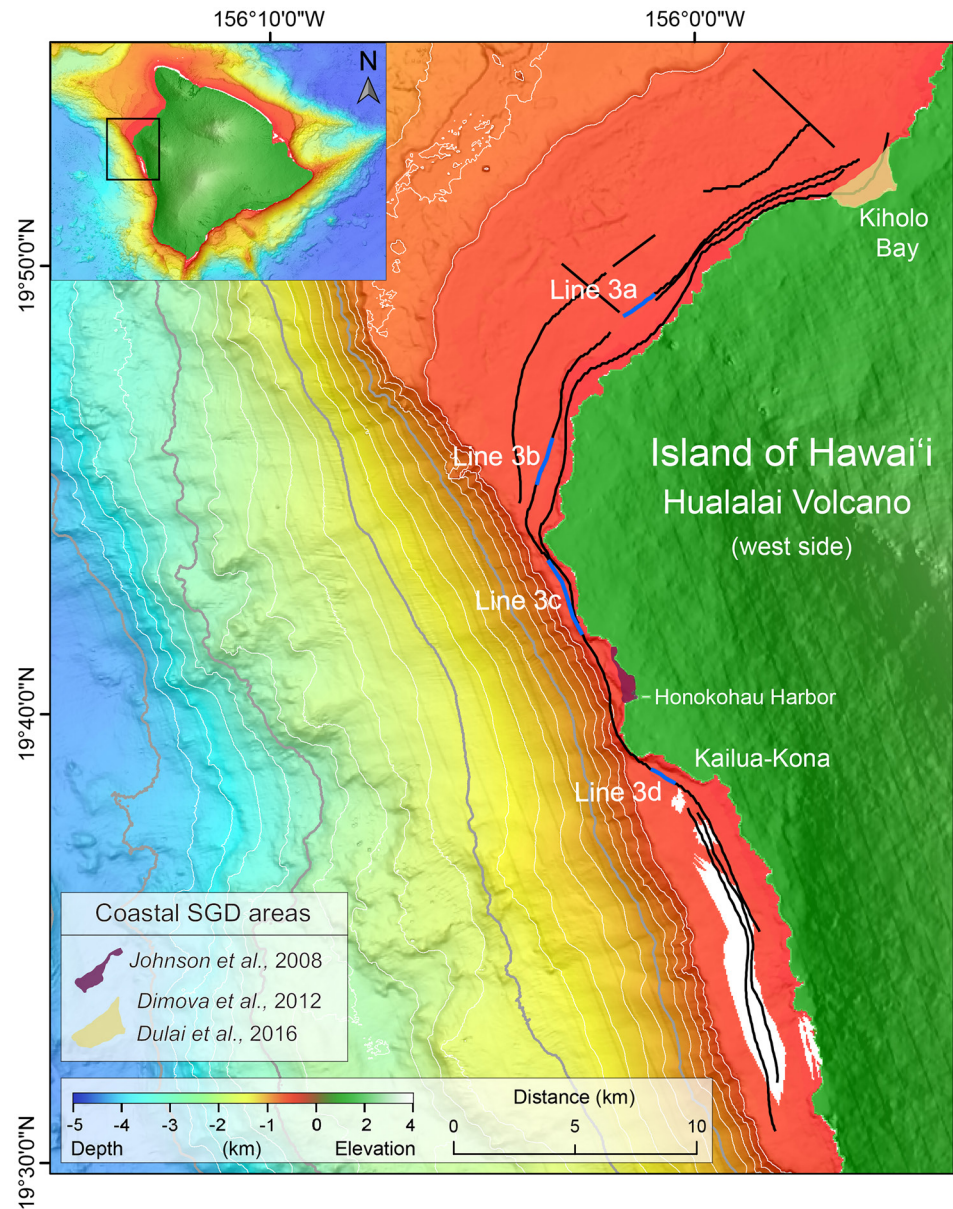
Figure 1. Map of the study area parallels the Hualalai terrestrial aquifer at Kailua-Kona, offshore west Hawai'i. The black lines denote the survey towlines (10 inlines and two crosslines). Blue lines represent regions where freshwater plumes were detected (Figures 2, 3, and S8). The purple and yellow polygons represent coastal SGD areas detected in previous studies. White lines denote depth contours of 200 m, and gray lines the depth contours of 1,000 m. Inset map: The island of Hawai'i, with a black rectangle indicating the main map area. The Hualalai terrestrial aquifer encompasses the entire map region. Areas with no bathymetry data are shown in white. Bathymetry data: Courtesy of Hawai'i Mapping Research Group.

faults, dikes, ash beds, lava tubes, and pyroclastic deposits, which compose Hawai'ias terrestrial, and submarine aquifers (Gingerich & Oki, 2000; Oki, 1999). The abundance of lava tubes in this region increases the volcanic rocks' permeability, thereby promoting large aquifers (Gingerich & Oki, 2000; Oki, 1999). The shallow region offshore Hawai'i surveyed in this study (Figure 1) is comprised of subaerial lava drapes, intermediately covered by coral reef terraces (J. G. Moore & Clague, 1987; Taylor, 2019), and low sediment content (see supporting information Figure S1). This volcanic formation enables freshwater flux from the sub-seafloor to the ocean.
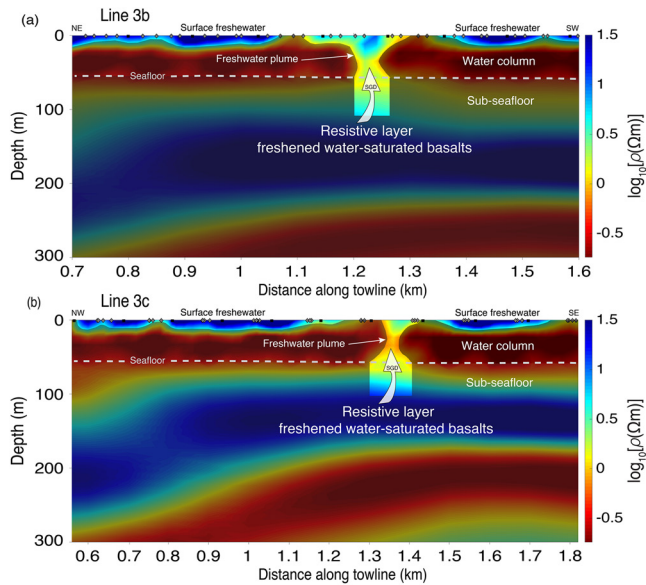
Figure 2. Two-dimensional inversion models derived from the CSEM data acquired in survey lines 3b and 3c. The color scale presents the electrical resistivity in $\log_{10}[\rho(\Omega m)]$. Black squares and gray diamonds denote transmitter and receiver positions, respectively. (a) Line 3b inversion model. The gray dashed line represents the seafloor, positioned at a water depth of ~50 m. Resistive freshwater plume imaged at a towline distance of ~1.23 km. The plume is most likely fed by SGD (white arrow) sourced from the sub-seafloor layer of freshened water-saturated basalts. Two lateral resistive anomalies from both flanks of the model represent surface freshwater bodies. We note that for enhanced visuality of the water column resistive anomalies, the resistivity shading thresholds are set to ~1.7 Ωm and ~6 Ωm for the plume and surface freshwater bodies, respectively. This inversion converged to an RMS misfit of 1.0 after 12 iterations. The amplitude and phase data error floors are 8%. (b) Line 3c inversion model. Moderate freshwater plume detected at a towline distance of ~1.35 km. The shallow lateral resistive anomalies represent surface freshwater bodies that extend up to 700 m. The resistivity shading thresholds are set to ~1 Ωm and ~6 Ωm for the plume and surface freshwater bodies, respectively. This inversion fits an RMS misfit of 1.0 after 14 iterations, with error floors of 8% and 6% for the amplitude and phase data.

SGD has a unique role in Hawai'i's ocean biogeochemistry, as it is the sole source of nutrients to the region's oligotrophic coastal waters (Johnson et al., 2008). The continuous influx of SGD to west Hawai'i coastline results in nutrient-rich brackish mixtures of fresh and seawater (Dimova et al., 2012; Dulai et al., 2016; Johnson et al., 2008). North Pacific Subtropical Gyre and Hawaiian archipelago interactions dominate the current dynamics in west Hawai'i via tidally-induced internal waves. These currents' governing direction is along-shore with an average magnitude of 0.05–0.1 m/s (Janeković et al., 2013).

2. Methods

2.1. Data Acquisition and Processing

In September 2018, we collected marine CSEM data using a surface-towed CSEM system to image the electrical resistivity structure of the submerged flank of the Hualalai volcano (Attias et al., 2020), as well as the oceanic water column offshore west of Hawai'i. Our survey included towlines parallel and perpendicular to the Hualalai terrestrial aquifer at incremental distances from the Kailua-Kona coastline, covering an offshore area of approximately 4 × 40 km, producing ~200 km of continuous CSEM data (Figure 1).

The surface-towed CSEM system employs a 40-m-long dipole antenna towed in ~0.5 m depth behind the survey boat at an average speed of 3.5 knots while transmitting a 100 A current. A doubly symmetric square waveform (Myer et al., 2011) at a fundamental frequency of 1 Hz with a sampling rate of 250 Hz generated a source dipole moment of 5.09 kAm (Attias et al., 2020). The survey boat surface-towed four broadband electromagnetic (EM) receivers at offsets 268, 536, 804, and 1,072 m. A Dorsal unit positioned 30 m behind the EM receivers array recorded the water depth and surface water conductivity/temperature. Each EM receiver recorded the inline horizontal electric field on a 2 m dipole positioned ~0.65 m below the ocean surface. GPS units positioned above sea level (timing accuracy of 10 ns) and electronic compasses logged the receiver positions and orientations, respectively.

The acquired CSEM data were Fourier transformed into the frequency domain and stacked over 60 s intervals. This stacking corresponds to ~20 m lateral distance between receiver stack points, producing high-density amplitude and phase responses as a function of position and frequency harmonics. The stacked amplitude and phase responses were then merged with the transmitter's and receiver's navigational information. For the CSEM inversion, we used the strongest harmonics of the doubly symmetric square waveform (Myer et al., 2011), here corresponding to frequencies of 3 and 7 Hz. These two frequencies produced quality data and high sensitivity to the electrical resistivity of the water column. In combination with high data density, the frequencies yielded high-resolution inversion models.

2.2. CSEM Inversion Parameterization

To invert the CSEM data for electrical resistivity, we employed the open-source MARE2DEM code, a 2-D nonlinear regularized inversion method that uses a parallel goal-oriented adaptive finite-element algorithm (Key, 2016). MARE2DEM employs Occam's inversion, which searches for the smoothest model that fits the data to a predefined root-mean-square (RMS) target misfit (Constable et al., 1987). Here, we used quality data with a high signal-to-noise ratio of 20, which led to irregular receiver spacing (Figures 2, 3a and s8a). The CSEM inversion-starting model discretization includes a 10^{13} Ωm air layer as a fixed-parameter, followed by finely discretized (20 m × 10 m) quadrilateral mesh for the water column (free parameters with
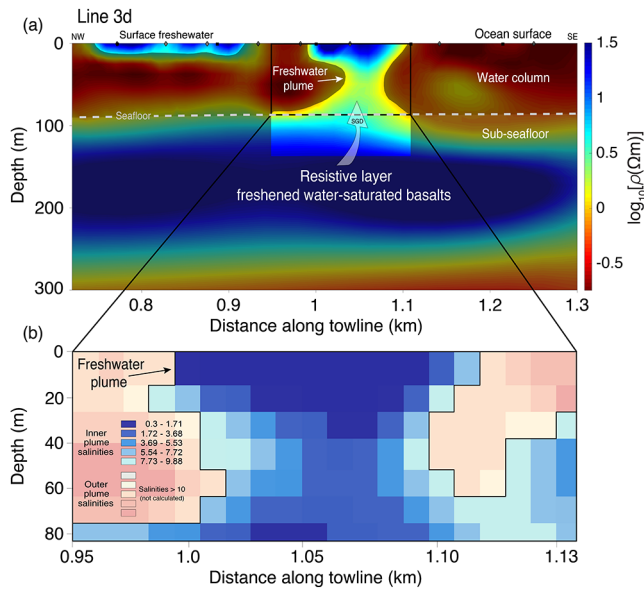
Figure 3. (a) Two-dimensional inversion model derived from the CSEM data acquired in survey line 3d. The color scale presents the electrical resistivity in $\log_{10}[\rho(\Omega m)]$. The gray dashed line represents the seafloor, positioned at a water depth of ~95 m. For enhanced visuality of the water column resistive anomalies, the resistivity shading thresholds are ~1.7 Ωm and ~6 Ωm for the plume and surface freshwater body, respectively. Distinctive freshwater plume imaged at a towline distance of ~1–1.1 km. This inversion converged to an RMS of 1.0 after 15 iterations, with error floors of 9% (amplitude) and 7% (phase) data. Black rectangular represents the water column plume area selected for salinity calculation. (b) Line 3d water column salinity distribution. The black line encompasses low salinities (<10) within the plume, calculated from the resistivity model. The average plume salinity is 4.4, with ~87% of freshwater. Salinities outside the plume were not calculated (see Section 2.3).

a starting value of 0.2 Ωm), and fine mesh elements for the sub-seafloor (1,000 m × 10 m), defined as free parameters (starting resistivity of 10 Ωm), as illustrated in supporting information Figure S2. Outside the region of interest, the model space quadrilateral mesh is 2-by-2 km. A high-resolution multibeam system recorded the bathymetry (supporting information Figure S1) used in the CSEM inversion modeling. The 40-m-long dipole transmitter and the 2 m-long towed EM receiver dipoles (Attias et al., 2020) were modeled as finite dipole lengths (Key, 2016). The inversions' starting horizontal-to-vertical roughness assigned to the models varies between 2 and 10 as a function of each model width-to-depth ratio. All of our CSEM inversion models fit the data to an RMS misfit of 1.0 with adequate model-to-data fits, yielding minimal and randomly distributed normalized residuals (see supporting information Figures S3–S5).

2.3. Resistivity-to-Salinity Calculation

The electrical conductivity (reciprocal of electrical resistivity) derived from our CSEM inversion models were converted to salinity profiles (Figures 3b and S8b) using the unitless Practical Salinity Scale 1978 (Lewis & Perkin, 1978). Salinity was calculated for each model cell extracted from the resistivity models. We then filtered the data points for salinities <10, thus solely yielding cells representing freshwater plume. By employing a 2-component mixing formula, we calculated the total volume of freshwater in each cell using Equation 1.

$$Sal\_mixed = f1 \times sal1 + f2 \times sal2 \tag{1}$$

where *Sal_mixed* represents the calculated (from resistivity) mixed salinity, *f*1 the volumetric fraction of pure freshwater, *sal*1 the salinity of pure freshwater, *f*2 the volumetric fraction of pure ocean water (*f*2 = 1 - *f*1), and *sal*2 the salinity of pure ocean water (assuming it equals to 35). For pure freshwater, we can assume that *sal*1 equals 0; therefore, Equation 1 can be rearranged to calculate the volumetric fraction of pure freshwater, as shown in Equation 2.

$$f1 = 1 - Sal\_mixed \,/\, sal2 \tag{2}$$

The resistivity-to-salinity conversion method applied here is theoretically robust. However, this method is limited in regions where the resistivity values are significantly small or significantly large. As resistivity values proceed toward minimal values, the resulting salinities approach infinity (see supporting information Figure S6). While measured resistivities cannot be zero, the step size effectively limits the method's ability to distinguish between different salinity values above ~10 (linear scale). Therefore, we chose 0.58 Ωm (salinity of 10) as the method lower sensitivity limit, as it represents the point in the resistivity-salinity curve where the salinity change per unit of resistivity change nears a vertical slope (supporting information Figure S6). Because of this relationship, salinities within a range of 11–35 cannot be distinguished. Consequently, regions (derived from CSEM inversions) with salinities of more than 10 were not calculated.

3. Results

The electrical resistivity structure of the sub-seafloor offshore west Hawai'i using all the survey lines shown in Figure 1 has been characterized by Attias et al., 2020. Here, we focus on 2-D isotropic CSEM inversion modeling of the water column using data collected at four sections of survey line 3 (Figure 1). Our CSEM models imaged electrically resistive freshwater plumes in high-resolution and unveiled spatially distributed anomalous resistive regions at the ocean surface, indicative of freshwater bodies (Figures 2 and 3). Daily pre/post survey conductivity, temperature, and depth (CTD) profiles detected multiple resistive anomalies
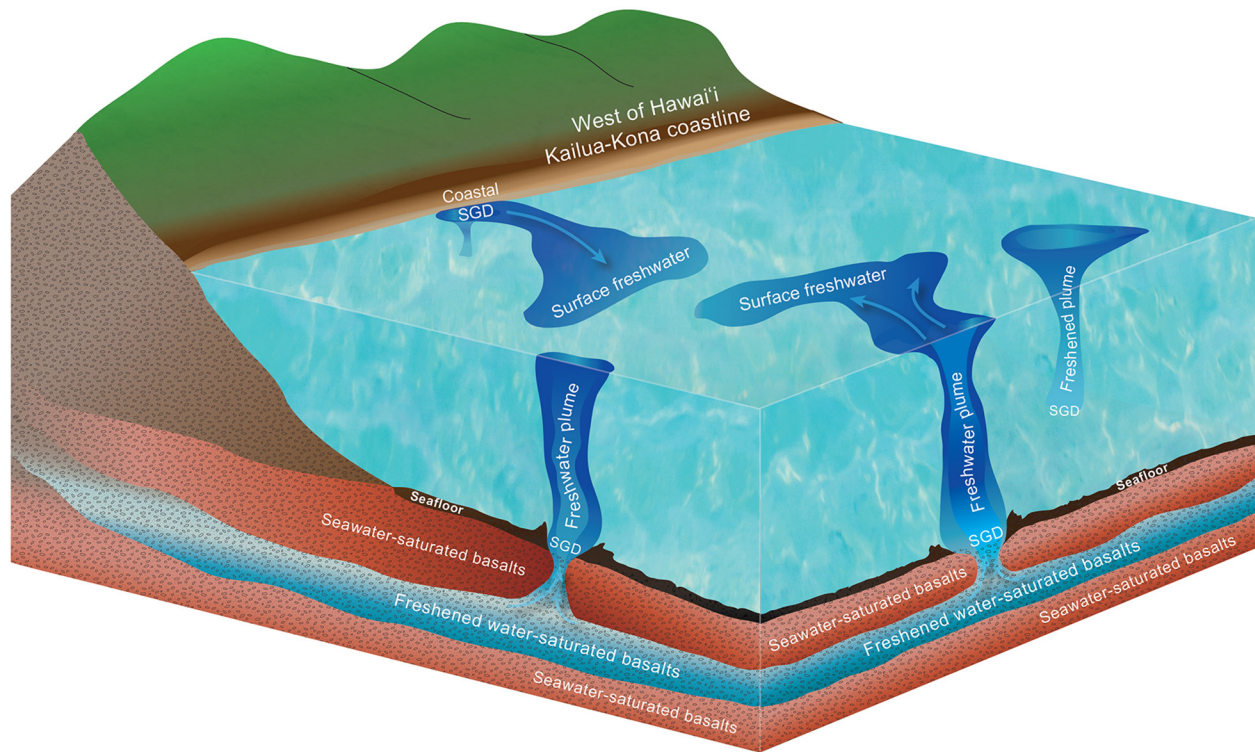
Figure 4. Conceptual model illustrating freshwater plumes and surface freshwater systems offshore west Hawai'i. Fresh groundwaters are transported from onshore to offshore through multilayer basaltic formation (Attias et al., 2020). From this sub-seafloor formation, freshened/freshwater migrate upward via porous/fractured seawater-saturated basalts, producing multiple large-scale vertical plumes that extend from the seafloor to the ocean surface. Surface freshwater bodies disconnected from plumes most likely result from nearby seeps or coastal SGD runoffs.

corresponding to notables decrease in salinities, which confirms the presence of freshwater plumes offshore west Hawai'i. The Jacobian sensitivity matrix (Farquharson & Oldenburg, 1996; MacGregor et al., 2001) derived from our inversion models demonstrate high data sensitivity to model parameters across the water column (supporting information Figure S7).

3.1. Electromagnetic Imaging of Freshwater Plumes

Survey line 3b (located ∼2 km from the coastline) electrical resistivity model presents a vertical feature with varying resistivity, ranging from ∼2 Ωm near the seafloor to ∼25 Ωm at the ocean surface (Figure 2a). We interpret this vertical resistor as a freshwater plume as the ocean background resistivity is ∼0.2–0.4 Ωm. Such plume-shaped freshwater features migrating vertically upward to the water column have been previously observed in continental shelves (Dimova et al., 2011; Kohout, 1966). This freshwater plume is ∼60 m wide at the seafloor and ∼130 m at the surface (Figure 2a). From both flanks of the model, two laterally elongated resistive anomalies (∼30 Ωm) extend from the surface to a depth of ∼15 m, indicating the presence of surface freshwater. The surface freshwater body from northeast of the plume most likely emerges from adjacent SGD point-sources or extend from coastal SGD, as it is disconnected from Line 3b plume (Figures 2a, 4). The model-to-data fit and normalized residuals of line 3b inversion are shown in supporting information Figure S3.

Similar to the electrical resistivity model of survey line 3b, the resistivity model of survey line 3c exhibits a central vertically elongated freshened (moderately brackish) water plume, with a resistivity range of ∼1–5 Ωm from the seafloor to the ocean surface, respectively (Figure 2b). This plume is ∼100 m wide at the seafloor and ∼80 m at the surface. Additionally, two laterally extensive surface freshwater bodies were detected, showing resistivity of ∼30 Ωm (Figure 2b). The surface freshwater body at the northwest flank of the model is disconnected from the plume. However, the southeast surface freshwater body is slightly linked to the plume, presenting a six times higher resistivity than the plume's surface resistivity (Figure 2b). This suggests

that the southeast surface freshwater body accumulates freshwater from nearby seeps, coastal SGD runoff, or line 3c plume (Figure 4). Supporting information Figure S4 shows the model-to-data fit and normalized residuals of line 3c inversion.

The electrical resistivity model of survey line 3d (located 0.5–1 km from the coastline) presents a prominent freshwater plume that is laterally extensive (∼200 m wide) above the seafloor and at the ocean surface but narrow at its center (Figure 3a). The plume's highest resistivity (∼30 Ωm) is between the surface and ∼25 m water depth, whereas near the seafloor, the water resistivity is ∼5 Ωm. The sub-seafloor freshened water layer (Attias et al., 2020) and the water column plume appears to be linked. However, the high resistivity detected at the upper plume part most likely results primarily from nearby SGD. At the northwest flank of the model, ∼30 Ωm resistive anomaly exists between the surface and ∼15 m depth, extending horizontally about 130 m (Figure 3a). This surface freshwater body is disconnected from line 3d plume, representing freshwater flux from nearby point-source discharge or coastal SGD runoff that drifted into line 3d profile (Figure 4). Figure s5 shows the model-to-data fit and normalized residuals of line 3d inversion. The electrical resistivity model of survey line 3a (located ∼2.3 km from the coastline) shows a freshened water plume (∼2.5 Ωm) that traverses the water column (supporting information Figure S8a). This plume is ∼100 m wide at the seafloor and ∼20 m at the surface. Figure s8a ideally demonstrates that a sub-seafloor freshened water layer (Attias et al., 2020) feeds this plume.

3.2. Plume Salinity Distribution and Freshwater Volumetric Estimation

We calculated the water column salinity distribution and freshwater volumetric estimation for the plumes entirely disconnected from surface freshwater bodies, as imaged by the resistivity models of survey lines 3d and 3a (Figures 3a and s8a). For this purpose, we used the unitless Practical Salinity Scale 1978 (Lewis & Perkin, 1978) to derive water column salinities that are less than 10 (see Section 2.3). The salinity distribution of line 3d plume region (206 m long, 83 m deep) was calculated using 4,242 points represented as model cells (Figure 3b). The total unit volume of the profile is 17,100 m^3. Note that unit volume refers to a profile thickness of 1 m. Salinities less than 10 were found in 2,762 model cells, representing a plume unit volume of 12,280 m^3. The inner plume calculated salinities ranged from 0.3 to 9.88 (Figure 3b), with an average salinity of 4.4. By applying the 2-component mixing equation (Section 2.3), we computed that the total freshwater unit volume for line 3d inner plume area is 10,720 m^3, composed of approximately 87% freshwater and 13% ocean water.

The salinity distribution of line 3a plume region (308 m long, 83 m deep; supporting information Figure S8b) was calculated using 6,204 points. The total unit volume of the profile is 23,400 m^3. Salinities less than 10 were found in 1,778 model cells, representing a plume unit volume of 7,473 m^3. The inner plume calculated salinities ranged from 0.5 to 9.85 (Figure s8b), with an average salinity of 5.3. The total calculated freshwater unit volume for line 3a inner plume area is 6,350 m^3. Such volume equates to a plume composition of about 85% freshwater and 15% ocean water.

4. Discussion

Terrestrial aquifers are one of Hawai'i's most critical natural resources, providing the majority of water for drinking, irrigation, domestic, commercial, and industrial needs, as well as coastal groundwater-dependent ecosystems (Duarte et al., 2010; Gingerich & Oki, 2000). Due to forecasted decreases in rainfall at areas under existing climate change projections (Timm et al., 2015; Zhang et al., 2016), increase in population, and agricultural demands in Hawai'i, it is essential to consider offshore freshwater discharges in future hydrogeologic models to optimize sustainable yields and aquifer storage calculations.

Hawai'i's SGD are typically point-source discharges (e.g., Johnson et al., 2008; Peterson et al., 2009) due to the nature of basalt aquifers preferential flow conduits channeling (Kreyns et al., 2020). Contrarily, SGD in clastic and karstic coastal aquifers present broad and diffusive seepage fields (e.g., Burnett et al., 2003; Moore & Wilson, 2005; Montiel et al., 2018). Multiple point-source SGD along the Kailua-Kona coastline are possibly linked to inland lava flow formations (Peterson et al., 2009; Dimova et al., 2012), manifested by sub-seafloor laterally continuous freshened groundwater reservoirs (Attias et al., 2020). Multichannel electrical resistivity measurements (Dimova et al., 2012) provide evidence for substantial coastal SGD via

well-defined freshwater conduits in Kiholo Bay (Figure 1). Such buoyant coastal SGD plumes can extend several hundred meters offshore, exhibiting sharp boundaries despite intense coastal mixing (e.g., Janeković et al., 2013; Johnson et al., 2008) — the offshore freshwater plumes we describe above present similar distinct boundaries.

Calculation of coastal SGD rates at west Hawai'i from surface thermal infrared imagery and point-source measurements suggests a total discharge that averages between 8,600 and 9,600 m^3/d [(Johnson et al., 2008; Dimova et al., 2012; Dulai et al., 2016), Figure 1]. Such discharge values are reasonably comparable with our estimation of the plumes unit volumes, assuming a residence time of approximately a day. These calculated volumes suggest that substantial SGD fluxes are required to produce sharply bounded, well-defined large freshened/freshwater plumes (Figures 2–4 and S8), to overcome the regional dynamic current field that generates effective mixing (Janeković et al., 2013). Nevertheless, it is difficult to estimate these freshwater plumes' flux rates due to the lack of parallel ocean currents and mixing observations. Such notable discharge is supported by water mass balance study (Hudson et al., 2018), which demonstrates that significant fresh groundwater recharge/discharge volumetric misbalance (∼40%) exists between the Hualalai aquifer groundwater recharge and coastal SGD along the corresponding Kailua-Kona shoreline. The observations above suggest that offshore submarine freshened water layers (Attias et al., 2020) are most likely renewable water sources, primarily dependent on rainfall patterns.

As the discharge locations and freshwater rates are highly heterogeneous, spatiotemporal estimates of SGD are essential for better managing water resources and predicting land-ocean boundary and water quality threats to coastal aquifers (Sawyer et al., 2016). For example, high-permeability conduits at this volcanic system (Kreyns et al., 2020) which enables the flow of groundwater offshore, also raise the risk of saltwater intrusion to the terrestrial aquifer (Geng & Michael, 2020). Our regional-scale CSEM mapping offshore west of Hawai'i shows the precise location of several individual SGD plumes and their spatial distribution from the seafloor to the ocean surface. This provides evidence of a complex hydrogeologic setting of multiple interbedded volcanic layers that channel fresh groundwater to deeper layers, allowing freshwater to discharge at a considerable distance from the coastline. Hence, characterizing SGD in a tectonic setting such as Hawai'i is of global importance since SGD rates in tectonically active margins are significantly greater than in passive margins (Zhou et al., 2019).

Here, we demonstrate that the CSEM method can effectively map offshore SGD. The capability of surface-towed CSEM to operate at a minimum water depth of ∼10 m provides a practical methodology to bridge the data gap related to distribution, extent, and dimensions of SGD across coastal transition zones. Therefore, combined with a suite of biochemical parameters (e.g., Rodellas et al., 2015), CSEM can help assess SGD effects on marine biogeochemistry at local and regional scales. However, to ideally evaluate the impact of nearshore/offshore SGD at different geologic settings [e.g., karstic submarine canyon (Paldor et al., 2020), carbonate rock aquifers (Holmden et al., 2012)], studies should also include CTD, nutrient, metal, and carbonate chemistry time-series measurements to derive freshwater fluxes, residence time, and seasonal variability.

5. Conclusions and Implications

Spatiotemporal variability of fresh SGD in coastal waters alters hydrologic processes, promotes primary production, supports food webs, changes stable isotope levels, and plays a prominent role in the global carbon budgets. Various geophysical, geochemical, and bioecological studies suggest that point-source SGD's in west Hawai'i are scattered across a large regional-scale. Our marine electromagnetic imaging reveals multiple offshore fresh SGD plumes, most likely fed by submarine freshened water layers. Plume-scale resistivity-to-salinity calculation and volumetric estimation infer that significant freshwater volumes accommodate these water column plumes, thus, highlighting the renewability nature of Hawai'i's hydrologic systems. Future hydrogeological models will benefit from incorporating offshore SGD to optimize aquifers' sustainable yields and storage calculations. This is the first study to demonstrate the CSEM method's capability to image and delineate freshwater plumes from the seafloor to the ocean surface in high-resolution. Thus, hydrogeologic, oceanographic, and biogeochemical studies can use marine CSEM to characterize complex, large-scale coastal water processes worldwide.

Data Availability Statement

The CSEM data are available for download at https://doi.org/10.4211/hs.e0a7f2a216e9456a8567b850db1cf1f9.

References

Attias, E., Thomas, D., Sherman, D., Ismail, K., & Constable, S. (2020). Marine electrical imaging reveals novel freshwater transport mechanism in Hawai'i. *Science Advances*, *6*(48), eabd4866. https://doi.org/10.1126/sciadv.abd4866

Bakken, T. H., Ruden, F., & Mangset, L. E. (2012). Submarine groundwater: A new concept for the supply of drinking water. *Water Resources Management*, *26*(4), 1015–1026. https://doi.org/10.1007/s11269-011-9806-1

Black, F. J., Paytan, A., Knee, K. L., De Sieyes, N. R., Ganguli, P. M., Gray, E., & Flegal, A. R. (2009). Submarine groundwater discharge of total mercury and monomethylmercury to central California coastal waters. *Environmental Science & Technology*, *43*(15), 5652–5659. https://doi.org/10.1021/es900539c

Burnett, W., Aggarwal, P., Aureli, A., Bokuniewicz, H., Cable, J., Charette, M., et al. (2006). Quantifying submarine groundwater discharge in the coastal zone via multiple methods. *The Science of the Total Environment*, *367*(2–3), 498–543. https://doi.org/10.1016/j.scitotenv.2006.05.009

Burnett, W., Bokuniewicz, H., Huettel, M., Moore, W., & Taniguchi, M. (2003). Groundwater and pore water inputs to the coastal zone. *Biogeochemistry*, *66*(1–2), 3–33. https://doi.org/10.1023/b:biog.0000006066.21240.53

Church, T. M. (1996). An underground route for the water cycle. *Nature*, *380*(6575), 579–580. https://doi.org/10.1038/380579a0

Cohen, D., Person, M., Wang, P., Gable, C. W., Hutchinson, D., Marksamer, A., et al. (2010). Origin and extent of fresh paleowaters on the Atlantic continental shelf, USA. *Groundwater*, *48*(1), 143–158. https://doi.org/10.1111/j.1745-6584.2009.00627.x

Constable, S. (2010). Ten years of marine CSEM for hydrocarbon exploration. *Geophysics*, *75*(5), 67–81. https://doi.org/10.1190/1.3483451

Constable, S. C., Parker, R. L., & Constable, C. G. (1987). Occam's inversion: A practical algorithm for generating smooth models from electromagnetic sounding data. *Geophysics*, *52*(3), 289–300. https://doi.org/10.1190/1.1442303

Cyronak, T., Santos, I. R., Erler, D. V., & Eyre, B. D. (2013). Groundwater and porewater as major sources of alkalinity to a fringing coral reef lagoon (Muri Lagoon, Cook Islands). *Biogeosciences*, *10*, 2467. https://doi.org/10.5194/bg-10-2467-2013

Dimova, N. T., Burnett, W. C., & Speer, K. (2011). A natural tracer investigation of the hydrological regime of Spring Creek Springs, the largest submarine spring system in Florida. *Continental Shelf Research*, *31*(6), 731–738. https://doi.org/10.1016/j.csr.2011.01.010

Dimova, N. T., Swarzenski, P. W., Dulaiova, H., & Glenn, C. R. (2012). Utilizing multichannel electrical resistivity methods to examine the dynamics of the fresh water-seawater interface in two Hawaiian groundwater systems. *Journal of Geophysical Research*, *117*(C2), C02012. https://doi.org/10.1029/2011JC007509

Duarte, T. K. e., Hemond, H. F., Frankel, D., & Frankel, S. (2006). Assessment of submarine groundwater discharge by handheld aerial infrared imagery: case study of Kaloko fishpond and bay, Hawai'i. *Limnology and Oceanography: Methods*, *4*(7), 227–236. https://doi.org/10.4319/lom.2006.4.227

Duarte, T. K., Pongkijvorasin, S., Roumasset, J., Amato, D., & Burnett, K. (2010). Optimal management of a Hawaiian Coastal aquifer with nearshore marine ecological interactions. *Water Resources Research*, *46*(11). https://doi.org/10.1029/2010wr009094

Dulai, H., Kamenik, J., Waters, C. A., Kennedy, J., Babinec, J., Jolly, J., & Williamson, M. (2016). Autonomous long-term gamma-spectrometric monitoring of submarine groundwater discharge trends in Hawaii. *Journal of Radioanalytical and Nuclear Chemistry*, *307*(3), 1865–1870. https://doi.org/10.1007/s10967-015-4580-9

Edwards, N. (2005). Marine controlled source electromagnetics: Principles, methodologies, future commercial applications. *Surveys in Geophysics*, *26*(6), 675–700. https://doi.org/10.1007/s10712-005-1830-3

Evans, R., & Key, K. (2016). Mapping Offshore Freshwater Deposits Using Electromagnetic Methods. In *Near Surface Geoscience 2016 - Second Applied Shallow Marine Geophysics Conference*. https://doi.org/10.3997/2214-4609.201602169

Farquharson, C. G., & Oldenburg, D. W. (1996). Approximate sensitivities for the electromagnetic inverse problem. *Geophysical Journal International*, *126*(1), 235–252. https://doi.org/10.1111/j.1365-246x.1996.tb05282.x

Fujita, K., Shoji, J., Sugimoto, R., Nakajima, T., Honda, H., Takeuchi, M., et al. (2019). Increase in fish production through bottom-up trophic linkage in coastal waters induced by nutrients supplied via submarine groundwater. *Frontiers in Environmental Science*, *7*, 82. https://doi.org/10.3389/fenvs.2019.00082

Geng, X., & Michael, H. A. (2020). Preferential flow enhances pumping-induced saltwater intrusion in volcanic aquifers. *Water Resources Research*, *56*(5), e2019WR026390. https://doi.org/10.1029/2019wr026390

Gingerich, S. B., & Oki, D. S. (2000). *Ground water in Hawaii (Vol. 126; Tech. Rep.)*. US Geological Survey.

Gleick, P. H., & Palaniappan, M. (2010). Peak water limits to freshwater withdrawal and use. *Proceedings of the National Academy of Sciences*, *107*(25), 11155–11162. https://doi.org/10.1073/pnas.1004812107

Gustafson, C., Key, K., & Evans, R. L. (2019). Aquifer systems extending far offshore on the US Atlantic margin. *Scientific Reports*, *9*(1), 1–10. https://doi.org/10.1038/s41598-019-44611-7

Haroon, A., Lippert, M., Mogilatov, V., & Tezkan, B. (2018). First application of the marine differential electric dipole for groundwater investigations: A case study from Bat Yam, Israel. *Geophysics*, *83*(2), B59–B76. https://doi.org/10.1190/geo2017-0162.1

Holmden, C., Papanastassiou, D. A., Blanchon, P., & Evans, S. (2012). δ44/40Ca variability in shallow water carbonates and the impact of submarine groundwater discharge on Ca-cycling in marine environments. *Geochimica et Cosmochimica Acta*, *83*, 179–194. https://doi.org/10.1016/j.gca.2011.12.031

Hudson, C., Dulai, H., & El-Kadi, A. (2018). Determining flow paths of submarine groundwater discharge on the kona cost, Hawai'i. In *Ocean sciences meeting*. Portland, Oregon.

Janeković, I., Powell, B., Matthews, D., McManus, M., & Sevadjian, J. (2013). 4D-Var data assimilation in a nested, coastal ocean model: A Hawaiian case study. *Journal of Geophysical Research: Oceans*, *118*, 5022–5035.

Jiao, J. J., Shi, L., Kuang, X., Lee, C. M., Yim, W. W.-S., & Yang, S. (2015). Reconstructed chloride concentration profiles below the seabed in Hong Kong (China) and their implications for offshore groundwater resources. *Hydrogeology Journal*, *23*(2), 277–286. https://doi.org/10.1007/s10040-014-1201-6

Johnson, A. G., Glenn, C. R., Burnett, W. C., Peterson, R. N., & Lucey, P. G. (2008). Aerial infrared imaging reveals large nutrient-rich groundwater inputs to the ocean. *Geophysical Research Letters*, *35*, L15606. https://doi.org/10.1029/2008gl034574

Key, K. (2016). MARE2DEM: A 2-D inversion code for controlled-source electromagnetic and magnetotelluric data. *Geophysical Journal International*, *207*(1), 571–588. https://doi.org/10.1093/gji/ggw290

Kim, I., & Kim, G. (2011). Large fluxes of rare earth elements through submarine groundwater discharge (SGD) from a volcanic island, Jeju, Korea. *Marine Chemistry*, *127*(1–4), 12–19. https://doi.org/10.1016/j.marchem.2011.07.006

Knee, K. L., Crook, E. D., Hench, J. L., Leichter, J. J., & Paytan, A. (2016). Assessment of submarine groundwater discharge (SGD) as a source of dissolved radium and nutrients to Moorea (French Polynesia) coastal waters. *Estuaries and Coasts*, *39*(6), 1651–1668. https://doi.org/10.1007/s12237-016-0108-y

Kohout, F. (1966). Submarine springs: A neglected phenomenon of coastal hydrology. *Hydrology*, *26*, 391–413.

Kreyns, P., Geng, X., & Michael, H. A. (2020). The influence of connected heterogeneity on groundwater flow and salinity distributions in coastal volcanic aquifers. *Journal of Hydrology*, *586*, 124863. https://doi.org/10.1016/j.jhydrol.2020.124863

Lewis, E. L., & Perkin, R. G. (1978). Salinity: Its definition and calculation. *Journal of Geophysical Research*, *83*(C1), 466–478. https://doi.org/10.1029/jc083ic01p00466

Luijendijk, E., Gleeson, T., & Moosdorf, N. (2020). Fresh groundwater discharge insignificant for the world's oceans but important for coastal ecosystems. *Nature Communications*, *11*(1), 1–12. https://doi.org/10.1038/s41467-020-15064-8

MacGregor, L., Sinha, M., & Constable, S. (2001). Electrical resistivity structure of the Valu Fa Ridge, Lau Basin, from marine controlled-source electromagnetic sounding. *Geophysical Journal International*, *146*(1), 217–236. https://doi.org/10.1046/j.1365-246x.2001.00440.x

Maher, D. T., Santos, I. R., Golsby-Smith, L., Gleeson, J., & Eyre, B. D. (2013). Groundwater-derived dissolved inorganic and organic carbon exports from a mangrove tidal creek: The missing mangrove carbon sink? *Limnology & Oceanography*, *58*(2), 475–488. https://doi.org/10.4319/lo.2013.58.2.0475

Manzoor, Q., Martin-Nagle, R., Oster, J., Lamizana, B., Voutchkov, N., KooOshimma, S., et al. (2020). *UN-water, 2020: UN-water analytical brief on unconventional water resources*. Geneva, Switzerland.

Mayfield, K. K., Eisenhauer, A., Ramos, D. P. S., Higgins, J. A., Horner, T. J., & Auro, M., et al. (2021). Groundwater discharge impacts marine isotope budgets of Li, Mg, Ca, Sr, and Ba. *Nature Communications*, *12*(1), 1–9. https://doi.org/10.1038/s41467-020-20248-3

Micallef, A., Person, M., Berndt, C., Bertoni, C., Cohen, D., Dugan, B., et al. (2020). Offshore freshened groundwater in continental margins. *Reviews of Geophysics*, *59*(1), e2020RG000706.

Micallef, A., Person, M., Haroon, A., Weymer, B. A., Jegen, M., Schwalenberg, K., et al. (2020). 3D characterisation and quantification of an offshore freshened groundwater system in the Canterbury Bight. *Nature Communications*, *11*(1), 1–15. https://doi.org/10.1038/s41467-020-14770-7

Michael, H. A., Post, V. E. A., Wilson, A. M., & Werner, A. D. (2017). Science, society, and the coastal groundwater squeeze. *Water Resources Research*, *53*(4), 2610–2617. https://doi.org/10.1002/2017wr020851

Montiel, D., Dimova, N., Andreo, B., Prieto, J., García-Orellana, J., & Rodellas, V. (2018). Assessing submarine groundwater discharge (SGD) and nitrate fluxes in highly heterogeneous coastal karst aquifers: Challenges and solutions. *Journal of Hydrology*, *557*, 222–242. https://doi.org/10.1016/j.jhydrol.2017.12.036

Moore, J. G., & Clague, D. (1987). Coastal lava flows from Mauna Loa and Hualalai volcanoes, Kona, Hawaii. *Bulletin of Volcanology*, *49*(6), 752–764. https://doi.org/10.1007/bf01079826

Moore, W. S. (1996). Large groundwater inputs to coastal waters revealed by 226Ra enrichments. *Nature*, *380*(6575), 612–614. https://doi.org/10.1038/380612a0

Moore, W. S. (2010). The effect of submarine groundwater discharge on the ocean. *Annual Review of Marine Science*, *2*, 345–347. https://doi.org/10.1146/annurev-marine-120308-081019

Moore, W. S., & Wilson, A. M. (2005). Advective flow through the upper continental shelf driven by storms, buoyancy, and submarine groundwater discharge. *Earth and Planetary Science Letters*, *235*(3–4), 564–576. https://doi.org/10.1016/j.epsl.2005.04.043

Moosdorf, N., & Oehler, T. (2017). Societal use of fresh submarine groundwater discharge: An overlooked water resource. *Earth-Science Reviews*, *171*, 338–348. https://doi.org/10.1016/j.earscirev.2017.06.006

Myer, D., Constable, S., & Key, K. (2011). Broad-band waveforms and robust processing for marine CSEM surveys. *Geophysical Journal International*, *184*(2), 689–698. https://doi.org/10.1111/j.1365-246x.2010.04887.x

Oki, D. S. (1999). Geohydrology and numerical simulation of the ground-water flow system of Kona, Island of Hawaii (*Tech. Rep.*, Vol. 70): U.S. Geological Survey US.

Paerl, H. W. (1997). Coastal eutrophication and harmful algal blooms: Importance of atmospheric deposition and groundwater as "new" nitrogen and other nutrient sources. *Limnology & Oceanography*, *42*(5, part 2), 1154–1165. https://doi.org/10.4319/lo.1997.42.5_part_2.1154

Paldor, A., Katz, O., Aharonov, E., Weinstein, Y., Roditi-Elasar, M., Lazar, A., & Lazar, B. (2020). Deep submarine groundwater discharge—evidence from Achziv submarine canyon at the exposure of the Judea group confined aquifer, Eastern Mediterranean. *Journal of Geophysical Research: Oceans*, *125*(1), e2019JC015435. https://doi.org/10.1029/2019jc015435

Person, M., Wilson, J. L., Morrow, N., & Post, V. E. A. (2017). Continental-shelf freshwater water resources and improved oil recovery by low-salinity waterflooding. *Bulletin*, *101*(1), 1–18. https://doi.org/10.1306/05241615143

Peterson, R. N., Burnett, W. C., Glenn, C. R., & Johnson, A. G. (2009). Quantification of point-source groundwater discharges to the ocean from the shoreline of the Big Island, Hawaii. *Limnology & Oceanography*, *54*(3), 890–904. https://doi.org/10.4319/lo.2009.54.3.0890

Post, V. E. A., Groen, J., Kooi, H., Person, M., Ge, S., & Edmunds, W. M. (2013). Offshore fresh groundwater reserves as a global phenomenon. *Nature*, *504*(7478), 71. https://doi.org/10.1038/nature12858

Prakash, R., Srinivasamoorthy, K., Gopinath, S., & Saravanan, K. (2018). Measurement of submarine groundwater discharge using diverse methods in Coleroon Estuary, Tamil Nadu, India. *Applied Water Science*, *8*(1), 13. https://doi.org/10.1007/s13201-018-0659-0

Rodellas, V., Garcia-Orellana, J., Masqué, P., Feldman, M., & Weinstein, Y. (2015). Submarine groundwater discharge as a major source of nutrients to the Mediterranean Sea. *Proceedings of the National Academy of Sciences of the United States of America*, *112*(13), 3926–3930. https://doi.org/10.1073/pnas.1419049112

Rosenberry, D. O., Duque, C., & Lee, D. R. (2020). History and evolution of seepage meters for quantifying flow between groundwater and surface water: Part 1–Freshwater settings, *Earth-Sci Review*, *204*, 103167.

Sawyer, A. H., David, C. H, & Famiglietti, J. S. (2016). Continental patterns of submarine groundwater discharge reveal coastal vulnerabilities. *Science*, *353*(6300), 705–707. https://doi.org/10.1126/science.aag1058

Sherman, D., Kannberg, P., & Constable, S. (2017). Surface towed electromagnetic system for mapping of subsea Arctic permafrost. *Earth and Planetary Science Letters*, *460*, 97–104. https://doi.org/10.1016/j.epsl.2016.12.002

Slomp, C. P., & Van Cappellen, P. (2004). Nutrient inputs to the coastal ocean through submarine groundwater discharge: Controls and potential impact. *Journal of Hydrology*, *295*(1–4), 64–86. https://doi.org/10.1016/j.jhydrol.2004.02.018

Starke, C., Ekau, W., & Moosdorf, N. (2020). Productivity and fish abundance at a submarine spring in a coastal lagoon on Tahiti, French Polynesia. *Frontiers in Marine Science*, *6*, 809. https://doi.org/10.3389/fmars.2019.00809

Stieglitz, T. (2005). Submarine groundwater discharge into the near-shore zone of the Great Barrier Reef, Australia. *Marine Pollution Bulletin*, *51*(1–4), 51–59. https://doi.org/10.1016/j.marpolbul.2004.10.055

Taniguchi, M., Dulai, H., Burnett, K. M., Santos, I. R., Sugimoto, R., Stieglitz, T., et al. (2019). Submarine Groundwater Discharge: Updates on its Measurement Techniques, Geophysical Drivers, Magnitudes and Effects. *Frontiers in Environmental Science*, *7*, 141. https://doi.org/10.3389/fenvs.2019.00141

Taylor, B. (2019). Shoreline slope breaks revise understanding of Hawaiian shield volcanoes evolution. *Geochemistry, Geophysics, Geosystems*, *20*, 4025–4045. https://doi.org/10.1029/2019gc008436

Timm, O. E., Giambelluca, T. W., & Diaz, H. F. (2015). Statistical downscaling of rainfall changes in Hawai'i based on the CMIP5 global model projections. *Journal of Geophysical Research: Atmospheres*, *120*, 92–112. https://doi.org/10.1002/2014jd022059

Valiela, I., Costa, J., Foreman, K., Teal, J. M., Howes, B., & Aubrey, D. (1990). Transport of groundwater-borne nutrients from watersheds and their effects on coastal waters. *Biogeochemistry*, *10*(3), 177–197. https://doi.org/10.1007/bf00003143

Zhang, C., Wang, Y., Hamilton, K., & Lauer, A. (2016). Dynamical downscaling of the climate for the Hawaiian Islands. Part I: Present day. *Journal of Climate*, *29*(8), 3027–3048. https://doi.org/10.1175/jcli-d-15-0432.1

Zhou, Y., Sawyer, A. H., David, C. H., & Famiglietti, J. S. (2019). Fresh Submarine Groundwater Discharge to the Near-Global Coast. *Geophysical Research Letters*, *46*, 5855–5863. https://doi.org/10.1029/2019gl082749